electronics

MDPI

Article

Enhancing Signal Recognition Accuracy in Delay-Based Optical Reservoir Computing: A Comparative Analysis of Training Algorithms

Ruibo Zhang [1,2], Tianxiang Luan [3], Shuo Li [1,2], Chao Wang [3] and Ailing Zhang [1,2,*]

[1] Engineering Research Center of Optoelectronic Devices & Communication Technology, Ministry of Education, Tianjin 300384, China; zrb300316@163.com (R.Z.); lishuo1866@163.com (S.L.)
[2] Key Laboratory of Film Electronic and Communication Devices, School of Electrical and Electronic Engineering, Tianjin University of Technology, Tianjin 300384, China
[3] School of Enginering, Univeristy of Kent, Canterbury CT2 7NT, UK; tl436@kent.ac.uk (T.L.); c.wang@kent.ac.uk (C.W.)
* Correspondence: alzhang@email.tjut.edu.cn

Abstract: To improve the accuracy of signal recognition in delay-based optical reservoir computing (RC) systems, this paper proposes the use of nonlinear algorithms at the output layer to replace traditional linear algorithms for training and testing datasets and apply them to the identification of frequency-modulated continuous wave (FMCW) LiDAR signals. This marks the inaugural use of the system for the identification of FMCW LiDAR signals. We elaborate on the fundamental principles of a delay-based optical RC system using an optical-injected distributed feedback laser (DFB) laser and discriminate four FMCW LiDAR signals through this setup. In the output layer, three distinct training algorithms—namely linear regression, support vector machine (SVM), and random forest—were employed to train the optical reservoir. Upon analyzing the experimental results, it was found that regardless of the size of the dataset, the recognition accuracy of the two nonlinear training algorithms was superior to that of the linear regression algorithm. Among the two nonlinear algorithms, the Random Forest algorithm had a higher recognition accuracy than SVM when the sample size was relatively small.

Keywords: delay-based optical reservoir computing; signal recognition; semiconductor laser; machine learning

Citation: Zhang, R.; Luan, T.; Li, S.; Wang, C.; Zhang, A. Enhancing Signal Recognition Accuracy in Delay-Based Optical Reservoir Computing: A Comparative Analysis of Training Algorithms. *Electronics* **2024**, *13*, 2202. https://doi.org/10.3390/electronics13112202

Academic Editor: Sergey Y. Yurish

Received: 4 May 2024
Revised: 28 May 2024
Accepted: 3 June 2024
Published: 5 June 2024

1. Introduction

The concept of artificial neural networks was introduced around the 1940s, representing a machine learning model that emulates the information processing mechanism of the brain. A recurrent neural network is a type of artificial neural network that may encounter problems such as vanishing or exploding gradients when processing long sequences [1]. To address these challenges, Jaeger and Maass introduced the echo state network (ESN) [2] and liquid state machine (LSM) [3] in 2001 and 2002, respectively. D. Verstraeten later synthesized these concepts in 2007, unifying them under the term "reservoir computing" [4]. RC has significantly streamlined the training process of recurrent neural networks and demonstrated impressive performance in various domains, including time series prediction [5], speech recognition [6], and pattern recognition [7]. RC has also expanded the potential for hardware implementation, thanks to its streamlined structure.

Delay-based optical RC is one of the hardware implementation approaches. Its advantage is that it significantly reduces the use of optical devices, thus simplifying the construction of hardware systems. Moreover, owing to the rapid transmission speed of optical signals, delay-based optical RC facilitates high-speed signal processing, fulfilling the speed requisites of contemporary communication and computing domains. In recent

years, delay-based optical RC has been proven to be immensely successful. For instance, delay-based optical RC has been applied in areas such as human activity recognition [8], handwritten digit recognition [9], and speech recognition [10]. In the current delay-based optical RC systems, the readout principle is based on ESNs, whereas in standard ESNs, the readout is linear and trained quickly by solving a convex optimization problem [11]. However, a linear readout might not possess sufficient representational power for modeling the embeddings derived from the reservoir states [12]. In the experiment of handwritten digit recognition, the accuracy rate of delay optics RC is only 83% [13], which is obviously lower than the accuracy rate that can be achieved by using convolutional neural networks [14]. For this reason, several authors have proposed replacing the linear algorithm with a nonlinear algorithm, such as SVMs [15] or Multilayer Perceptron (MLPs) [16,17]. Compared to linear algorithms, training with nonlinear algorithms can greatly enhance the performance of the system [18]. However, when MLP handles large-scale data and complex problems, the training time is long and the adjustment of related hyperparameters is complex, which contradicts our original intention of using the RC system. In comparison, the random forest algorithm is more in line with our requirements. As an ensemble learning algorithm composed of multiple decision trees, it can handle high-dimensional data and nonlinear relationships, has strong robustness, and is not prone to overfitting. Importantly, its training time is shorter than that of MLP. Therefore, in terms of the choice of nonlinear algorithms, we compare SVM and random forest algorithms with traditional linear algorithms. The test task is the recognition of FMCW LiDAR signals.

In the first section of this study, we elucidated the background of delay-based optical RC and the significance of this experiment in our research. In the second section of this study, we built a delay-based optical RC system and elaborated on the experimental principle and system model of delay optics RC. In the third section of this study, we compared the accuracy of linear and nonlinear algorithms for recognizing the same signal. The experimental results highlight the superior recognition accuracy achieved by nonlinear algorithms compared to that of linear algorithms. Furthermore, we compared the accuracy of two nonlinear algorithms in system recognition and found that there are differences in waveform recognition accuracy between nonlinear algorithms. Lastly, an optimized output layer training algorithm for delay-based optical RC is identified through experiments. Section 4 provides a comprehensive summary.

2. Principle and System Model

The delay-based optical reservoir computing and electronic reservoir computing are structurally the same, both consisting of three parts: the input layer, the reservoir layer, and the output layer. The pre-modulated signal is input to the MZM from the AWG, and the optical carrier emitted from the TL is modulated by the modulation voltage of the MZM. At this time, the MZM is in the operating state of intensity modulation. The output of the MZM is delivered to the delayed feedback loop after the PC modulates the polarization state of the optical path. In the loop, the current input is mixed with the input of the previous moment and injected into the DFB as a new input. The output of the DFB is the virtual node state x(t). One part of the output passes through the feedback loop, is combined with the input of the next moment, and is injected into the loop as a new input. The other part of the DFB's output, which is amplified by the EYDFA, is once again divided into two parts, and a part of the light is received by the OSA to view the working state of the system. The other part of the light is converted to an electrical signal by the PD and received by the DSA for collecting the virtual node state x(t). An experimental structure of the delay-based optical RC for signal recognition tasks is shown in Figure 1.

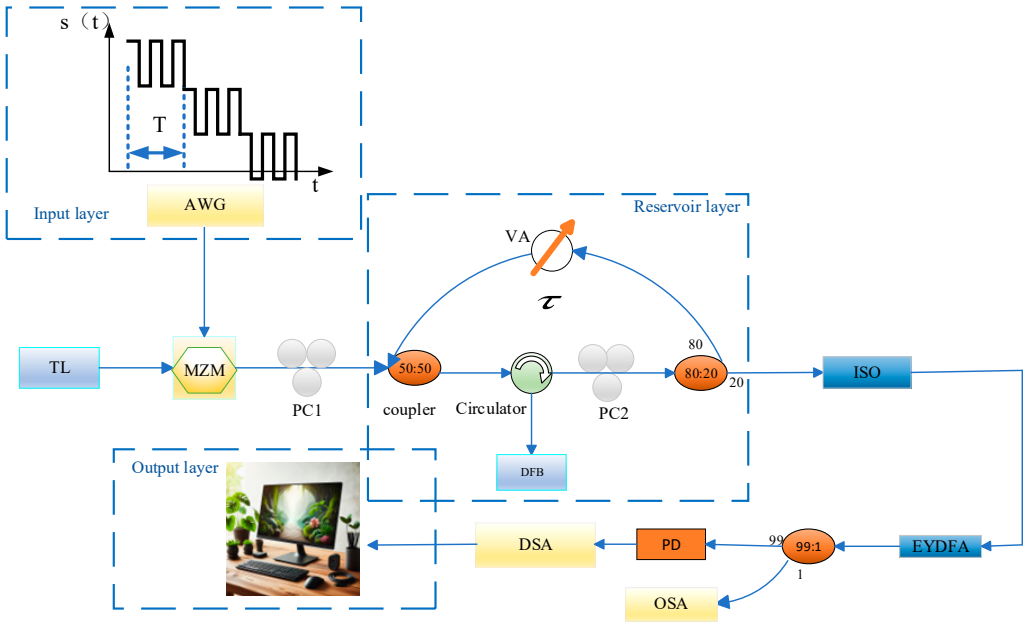

Figure 1. Experimental structure of the delay-based optical reservoir computing. TL: tunable laser, AWG: arbitrary waveform generator. MZM: Mach-Zehnder modulator, VA: variable attenuator, DSA: digital signal oscilloscope, DFB: distributed feedback laser, ISO: isolator, PC: polarization controller, PD: Photodetector, OSA: optical spectrum analyzer, EYDFA: erbium/ytterbium co-doped fiber amplifier.

2.1. Input Layer

The input layer is responsible for the process of modulating the input signal on the optical carrier. In order to keep the system in a perpetually disturbed state, we need to add a mask to the input signal u(t), as shown in Figure 2. The sampling time of the input signal u(t) is T. By introducing a mask with a period of T and multiplying it with the input signal, we can obtain the pre-modulated signal s(t). Usually, the mask can be different types of signals, such as digital masks, chaotic masks, and colored noise masks. The addition of the mask is equivalent to changing the input weight from the input signal to the reservoir layer. At the same time, the sampling interval of the mask plays a crucial role in the performance of the RC system. When θ is much less than T_R (where T_R is the characteristic time scale of the delay RC system), the diversity of virtual nodes will significantly decrease. When θ is greater than T_R, the state of the virtual node cannot fully reflect the transient response of the nonlinear node. For delay-based optical RC, the optimal interval between virtual nodes is approximately 0.2 times the system's characteristic time scale.

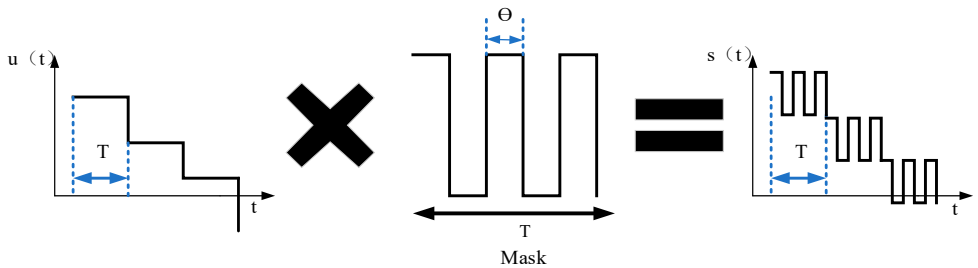

Figure 2. Applying a mask in the input layer.

The input signal, after being mask-modulated, is injected into the Mach–Zehnder modulator (MZM) by the AWG, and then the optical carrier emitted by the TL is injected into the reservoir layer. Tunable lasers are also called driven lasers [19].

2.2. Reservoir Layer

We employed a DFB and a feedback loop to form the reservoir layer. The dynamics of such a delay system exhibit high dimensionality and memory. This aligns well with the requirements of the RC system. In a feedback loop of length τ, there are N virtual nodes with a time interval of θ. When τ equals T, θ can be expressed as $\theta = \tau/N$, N is analogous to the nodes in a traditional reservoir layer. The values of the delayed variable at each of the N points define the states of the virtual nodes, which show the transient response of the reservoir when the input information is at a specific time. The state equation of the virtual nodes in the reservoir layer can be expressed as

$$x(t) = f[w_{in}u(t) + w_{res}x(t-1)] \tag{1}$$

In Equation (1), f represents the nonlinear mapping of the system. The system's nonlinear mapping is primarily manifested in the neurons' nonlinear activation functions. This nonlinear mapping is a key component of the neural network model, enabling the model to capture and process complex data patterns. Specifically, nonlinear mapping can generate nonlinear transfer function effects through certain optical devices. w_{in} represents the input weight brought by the mask, w_{out} represents the link weight between the virtual nodes inside the RC, $u(t)$ represents the current input signal, and $x(t-1)$ represents the signal of the feedback loop at the previous moment.

The working state of DFB is crucial throughout the entire reservoir layer. The working state of DFB is determined by the detuning frequency. The detuning frequency is the frequency difference before the master-slave laser. When the DFB laser operates in a stable injection-locking state, the RC system can demonstrate high consistency and memory ability [20]. As shown in Figure 3, the parameter space diagram of injection ratio and frequency detuning shows the distribution of the DFB system between injection-locked and unlocked states. In order to ensure that the DFB laser operates in a stable locked state, the best range of detuning frequency values is between -5 GHz and 0 GHz.

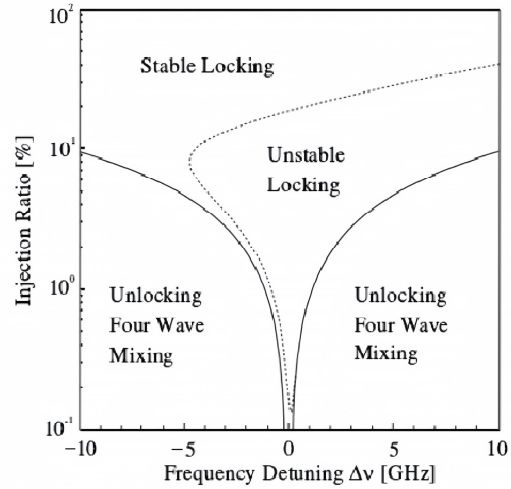

Figure 3. Distribution map of injection locking and unlocking regions in DFB.

The detuning frequency is determined by the wavelength difference between the master and slave lasers. In this experiment, the DFB laser outputs a fixed wavelength under specific temperature and current conditions, so we need to adjust the TL to achieve the optimal detuning frequency. Each time we change the output wavelength of the TL, we observe the spectrum in the OSA to determine whether the system has entered the injection-locked state. As shown in Figure 4, this indicates that the output wavelength of the DFB laser is injection-locked to the TL, and the wavelength of the main laser is 1548.632 at this time. The wavelength difference between the master and slave lasers is 0.032 nm, corresponding to a detuning frequency of -4 GHz.

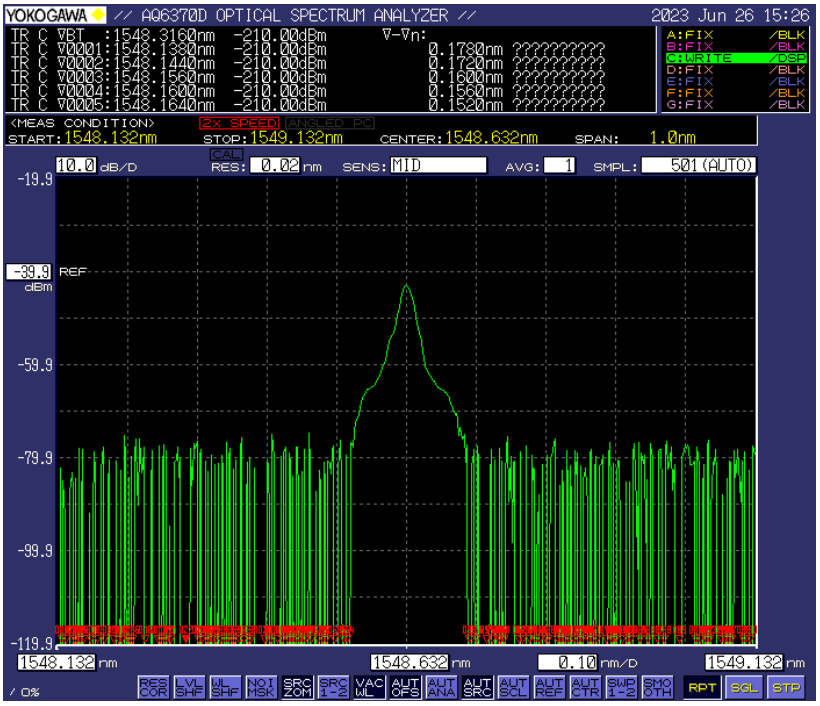

Figure 4. The working condition of the DFB laser captured by the OSA.

Feedback delay is a crucial indicator for delay-based optical RC systems. In this experiment, the feedback delay is determined by the length of the loop. If the circuit length is too large, it will result in the virtual node's state not fully reflecting the transient response of the nonlinear node. If the circuit length is too small, the diversity of virtual nodes will decrease, leading to a decrease in system performance. To ensure the memory of the system, we need to ensure that the clock cycle is about 3 to 4 times the feedback loop delay [21]. Therefore, it is very necessary to measure the delay of the feedback loop.

Initially, a square wave signal with a frequency of 1 MHz and a duty cycle of 0.005 was generated using MatlabR2021b, which was equivalently transformed into a signal that produces a pulse every 1 µs. Subsequently, a Fiber Bragg Grating (FBG) with a reflection wavelength of 1557.908 nm was used to replace the position of the DFB in Figure 1, as illustrated in Figure 5.

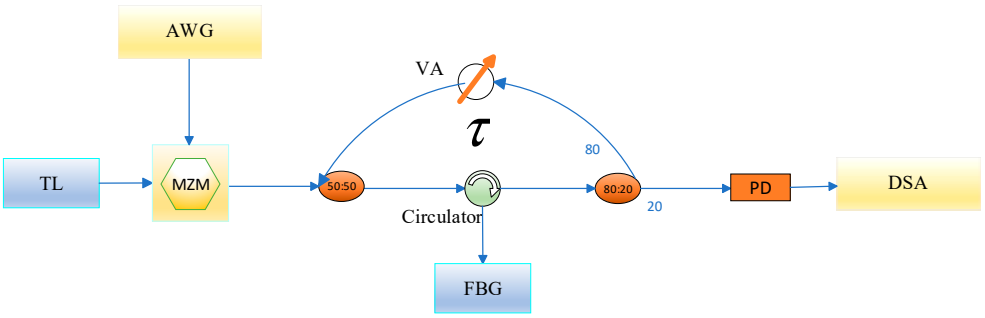

Figure 5. Measurement feedback delay schematic diagram.

The square wave was injected into the optical carrier with a wavelength of 1557.908 nm by the AWG, and after being reflected by the FBG, it was split into two by the 80:20 coupler. A portion of the light was fed back to the 50:50 coupler, while the other part was output to the oscilloscope through the PD. Due to the period of the square wave signal being 1 µs, the feedback signal will reappear when the current signal passes through the 80:20 coupler before the next square wave arrives until the power loss is exhausted. That is to say, there

will be pulses with smaller power between two equivalent pulses spaced 1 μs apart. The time interval between the large pulse and the small pulse is the current feedback delay of the system, as shown in Figure 6, measured to be 88 ns.

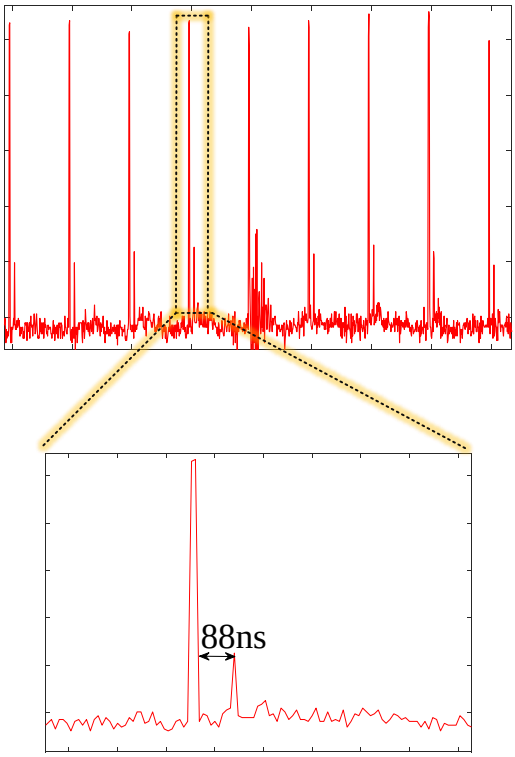

Figure 6. Pulse interval. The dashed box indicates the result of zooming in on a single cycle.

Given the inherent length of the FBG, it is necessary to calculate the time that light consumes in the FBG. With the FBG length being 0.8 m, the time can be determined as 8 ns based on the formula for light propagation distance in the fiber. Therefore, the actual delay of the RC system is 80 ns.

2.3. Output Layer

The output layer involves a post-processing procedure. In the current delay optical reservoir computing system, the output layer typically requires a photodetector to transform the state of the virtual nodes in the reservoir from the optical domain to the electrical domain. Then, a digital oscilloscope is used to collect the state of the virtual nodes. Ultimately, the output connection weights are determined based on a linear regression algorithm on a computer in an offline manner to complete the training process. During the testing process, the predicted output is calculated based on the state of the virtual nodes collected by the digital oscilloscope and the output connection weights determined during the training process. The training equation for its output layer can be represented as

$$y(t) = f_{out}[w_{out}x(t)] \tag{2}$$

In Equation (2), $y(t)$ represents the output result of the output layer, w_{out} represents the output connection weight, which is the parameter we need to determine through training, and f_{out} is the output function.

Upon completion of the training process for RC, we used the accuracy rate (AR) to evaluate the system's classification results on the test set and visualized the accuracy of each classification by drawing a confusion matrix. For the linear regression algorithm, we can also

represent the performance of the system by calculating the normalized root mean square error (NRMSE). AR and NRMSE can be represented by Equations (3) and (4), respectively:

$$AR = \frac{\text{Number of correctly classified items}}{\text{Total number of samples}} * 100\% \quad (3)$$

$$NRMSE = \frac{\sqrt{\frac{1}{n}\sum_{i=1}^{n}(y_i - \hat{y}_i)^2}}{y_{\max} - y_{\min}} \quad (4)$$

In Equation (4), y_i represents the ith observed value, $\hat{y}_i$ represents the ith predicted value, n represents the number of samples, and $y_{\max}$ and $y_{\min}$ represent the maximum and minimum values of the observed values, respectively.

In this experiment, we used linear regression, SVM, and random forest algorithms as the training algorithms for the output layer. The advantage of the linear regression algorithm is that it is simple to use and has low computational complexity. When the number of sampling points for the data to be calculated is N, the computational load required by FFT is $N \log_2 N$, but the computational load of linear regression is only N [22,23]. SVM has advantages in dealing with high-dimensional data and nonlinear problems. It has been successfully applied to radar signal recognition [24]. Random Forest is a comprehensive learning classification method that combines multiple trees for integrated prediction. Therefore, it can handle high-dimensional large data samples, and few parameters need to be adjusted during the training process. This method has excellent performance in terms of recognition accuracy, classifier stability, and model generalization capabilities [25]. In the following sections, we delve into the working principles of three distinct algorithms.

The fundamental concept of linear regression is to delineate the relationship between the dependent and independent variables by identifying an optimal fit line. Its basic form is expressed as follows:

$$y = a_1x_1 + a_2x_2 + \ldots + a_nx_n + b \quad (5)$$

In Equation (5), y denotes the target variable we aspire to predict, $x_1, x_2, \ldots, x_n$ signify the feature variables, $a_1, a_2, \ldots, a_n$ are the model parameters that represent the extent of influence each feature exerts on the prediction outcome, and b is the bias term. The objective of linear regression is to utilize methods such as gradient descent or least squares to identify a set of parameters that minimizes the discrepancy between the predicted y and the actual y.

The SVM algorithm encompasses three fundamental concepts: support vectors, margin, and hyperplane. Support Vectors: In a two-dimensional space, support vectors are the points closest to the hyperplane. In higher-dimensional spaces, support vectors are the vectors that are nearest to the hyperplane. Margin: The margin is the distance from the support vectors to the hyperplane. The objective of SVM is to find a hyperplane that maximizes this margin, resulting in what is known as the maximum margin hyperplane. Hyperplane: In a two-dimensional space, a hyperplane is a straight line used to split the data into two parts. In higher-dimensional spaces, a hyperplane can be a plane or a multidimensional space. A salient feature of the SVM algorithm is its reliance solely on support vectors, rather than on sample points far from the hyperplane. This endows SVM with robustness.

Random Forest is a bagging ensemble learning algorithm based on decision tree model classifiers, as shown in Figure 7. Its fundamental principle involves random sampling of the original data based on preset parameters, resulting in M-independent sub-sample datasets that have the same sample size as the original data. Feature extraction is then performed, with N feature variables randomly selected in each training set. The M sub-sample datasets serve as training samples to construct M decision tree models, forming a decision forest. When predicting test set data, the M decision tree models will yield M prediction results. Based on vote counting, the final prediction category is the mode of the M prediction results.

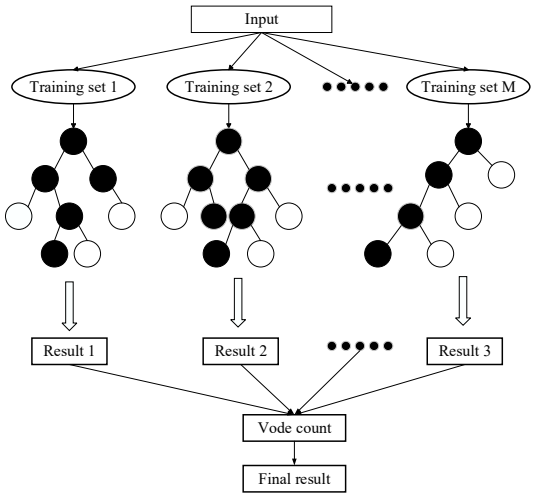

Figure 7. Classification principle of random forest.

3. Experiment Setup and Results

This section is divided into two parts. The first part describes the generation of the FMCW LiDAR waveforms and the construction of the delay-based optical RC system. The second part describes the impact of different algorithms in the output layer on the accuracy of the recognition results.

3.1. Experiment Setup

FMCW LiDAR usually adopts optical heterodyne coherence detection. After the signal light is coupled with the reference light, intermediate frequency (IF) signal carrying distance and speed information are generated after PD. Then, a very narrow power peak can be found in the power spectrum after the fast Fourier transform (FFT) of the IF signal so as to demodulate the accurate distance and speed information. However, in fact, almost all frequency-sweeping light sources cannot achieve ideal linear frequency sweeping. The nonlinearity of the frequency sweeping will seriously disturb the FFT peak and cause spectrum broadening, which will greatly reduce the resolution and SNR of the LiDAR and even fail to recognize the target [26]. Several approaches have been proposed to solve this problem. The first kind of method is frequency sampling by attaching an auxiliary interferometer that generates a clock signal with equal frequency intervals to trigger the data acquisition [27,28]. On the one hand, this method will increase the complexity of the system. On the other hand, in order to satisfy the Nyquist sampling theorem, the length of the auxiliary interferometer will limit the measurement range [29]. The second kind of method is resampling the original data by various algorithms such as zero-crossing interpolation and non-uniform FFT [30,31]. Although these resampling algorithms are low-cost and greatly compensate for the nonlinearity of the sweep, they are very complex and result in a significant increase in signal processing time. However, it is worth noting that, although spectrum broadening makes FFT peaks undistinguishable, it also makes the corresponding time domain waveforms more complex. And different distances will inevitably bring changes in the time domain waveform. Therefore, we decided to use the constructed delay-based optical RC system to identify the time-domain waveforms of the FMCW LiDAR.

The generation of FMCW LiDAR is shown in Figure 8. As depicted in Figure 8a, this segment utilizes a nonlinear chirped signal as the wavelength-scanning light source. The starting frequency of the chirped signal is 1 MHz, the cutoff frequency is 11 MHz, and the duration is 20 μs. The signal, upon encountering a coupler, was split into two distinct beams. The first beam, post-isolation, was channeled toward the target via a collimator, and its reflection was subsequently collected. The second beam acted as the reference light; it merged with the reflected beam and, following processing through a PD, culminated in

the formation of the intermediate frequency (IF) signal. The reference light representing different distances caused corresponding changes in the IF signal, as illustrated in Figure 8b.

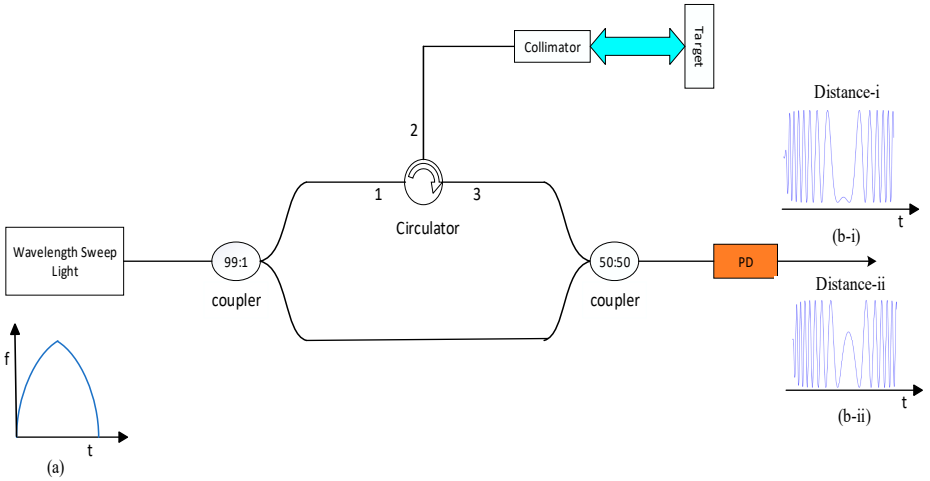

Figure 8. Schematic of the FMCW LiDAR system. (**a**) is a nonlinear sweep frequency light source, (**b-i**) and (**b-ii**) is two different radar signals at different distances.

Afterward, we need to preprocess these four signals by adding a mask. The mask is a pseudorandom binary mask generated by MatlabR2021b, with a duration T of 20 ns. In the 20 ns duration of the masking signal, there are a total of 200 sampling points. This implies that the sampling interval between adjacent mask points is 0.1 ns. Consequently, in the time-delay optical RC circuit, there are 200 virtual nodes with a spacing of 0.1 ns. Our objective is to insert the mask between each sampling point of the four signals in Figure 9, thereby forming our pre-modulated signal s(t), as depicted in Figure 10.

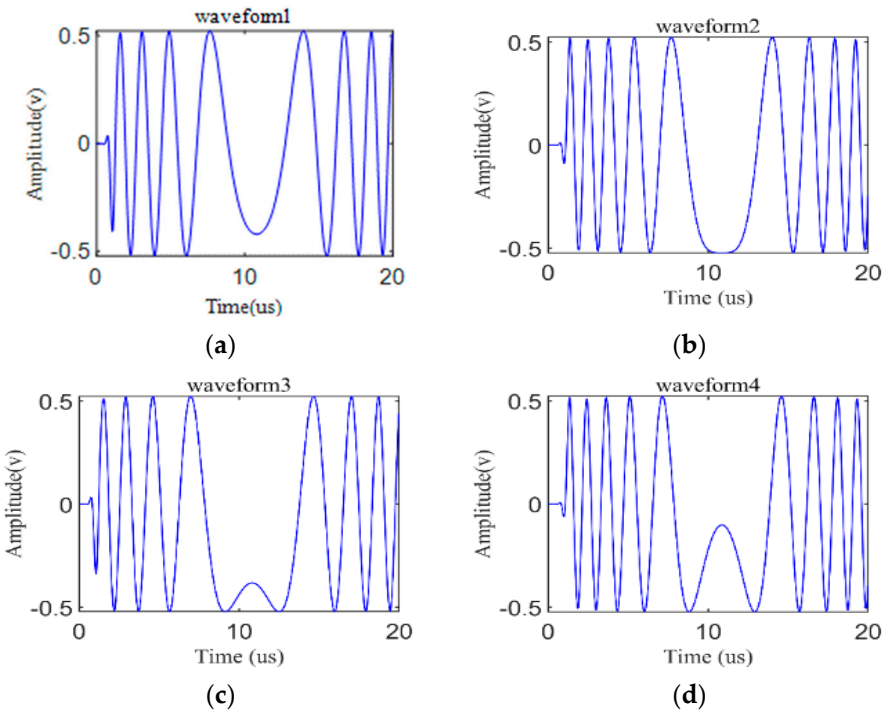

Figure 9. Four types of input signals. (**a**–**d**) are the FMCW LiDAR signals at four different distances generated by simulating the experimental principle in Figure 8 using MatlabR2021b.

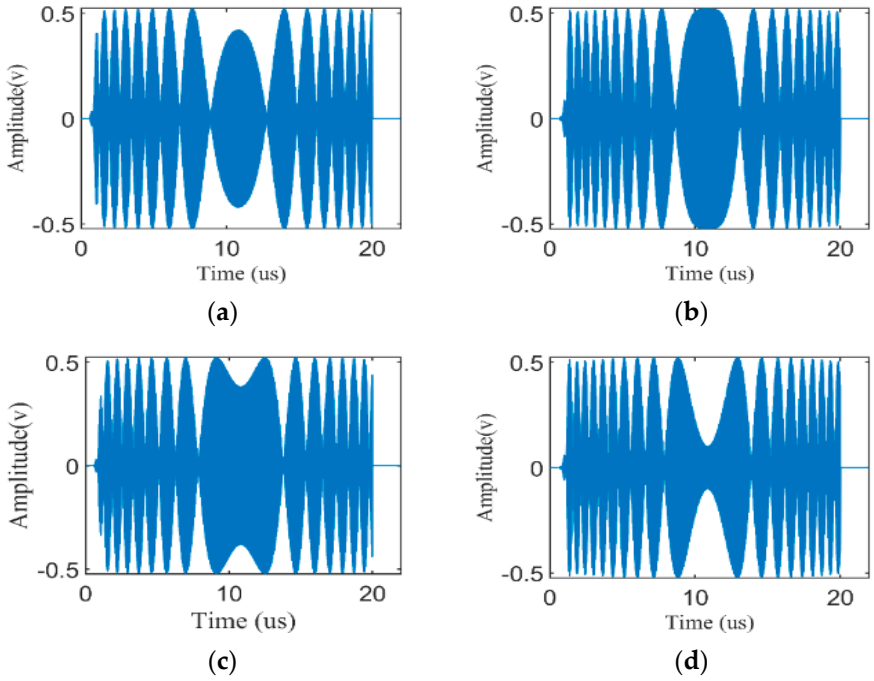

Figure 10. Four types of pre-modulated signals. (**a**–**d**) represent the pre modulated signal formed by adding masks to the four signals in Figure 9.

To facilitate the differentiation of adjacent signal cycles on the oscilloscope, we appended a 2 μs zero signal to the preprocessed signals.

In fact, the determination of the mask duration T and the sampling interval θ is based on the characteristic time scale of the system. The characteristic timescale of the system is the reciprocal of the relaxation oscillation frequency of the laser. As shown in Figure 11, the measured relaxation oscillation of the laser is 8.51 GHz. Therefore, the characteristic time scale of the system is approximately 0.12 ns. In order to keep the system in a state of disturbance and considering the highest sampling rate of the AWG device, we set θ to 0.1 ns. The value of the mask period T is related to the feedback delay τ of the delay optics RC. In the delay reservoir computing proposed by Appeltant et al. in 2011 [32], T and τ are in resonance, that is, $T \approx \tau$. However, this constraint is disadvantageous for the system, which is also confirmed in the research of Hülser et al. [21]. The resonance of the clock period T and the feedback delay τ will instead reduce the memory capacity of the system. In this experiment, we set $\tau = 4$ T. τ is 80 ns. Therefore, the value of the clock period T was set to 20 ns.

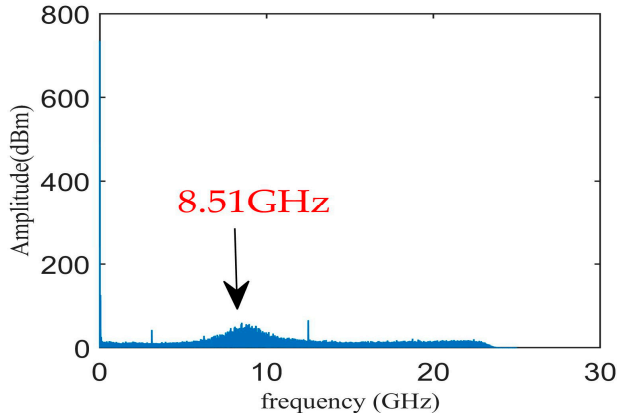

Figure 11. Frequency of relaxation oscillations in the DFB laser.

Finally, we need to inject the preprocessed signal from Figure 10 into the established delay optics RC system through AWG, with the sampling rate of AWG set to 10 GSa/s. Figure 1 illustrates the experimental structure. TL is the driving laser, with an output wavelength of 1548.632 nm and an output power of 14 dBm. The modulated signal was injected into the DFB laser through the PC, which was used to adjust the polarization state of the light. The DFB laser served as the response laser, with a bias current of 15 mA. When the temperature was set to 20 °C, the output wavelength of the laser was 1548.600 nm. At this time, the bias current was 1.07 times the threshold current of the DFB. The detuning frequency of the drive laser and the response laser was −4 GHz. In the feedback loop, the tunable attenuator adjusted the feedback power to −10 dBm. The feedback signal and the modulated signal at the next moment formed a new signal that was injected into the DFB laser.

The state of the virtual node is read by the DSA after the light signal was amplified by the erbium-doped fiber amplifier and then converted into an electrical signal by the PD. Specifically, the sampling rate of the DSA was set to 50 GSa/s. In order to collect as many signal cycles as possible, we set the sampling time of the DSA to 200 µs, which means that we could collect a complete waveform of eight cycles each time. The collection results of the DSA are shown in Figure 12.

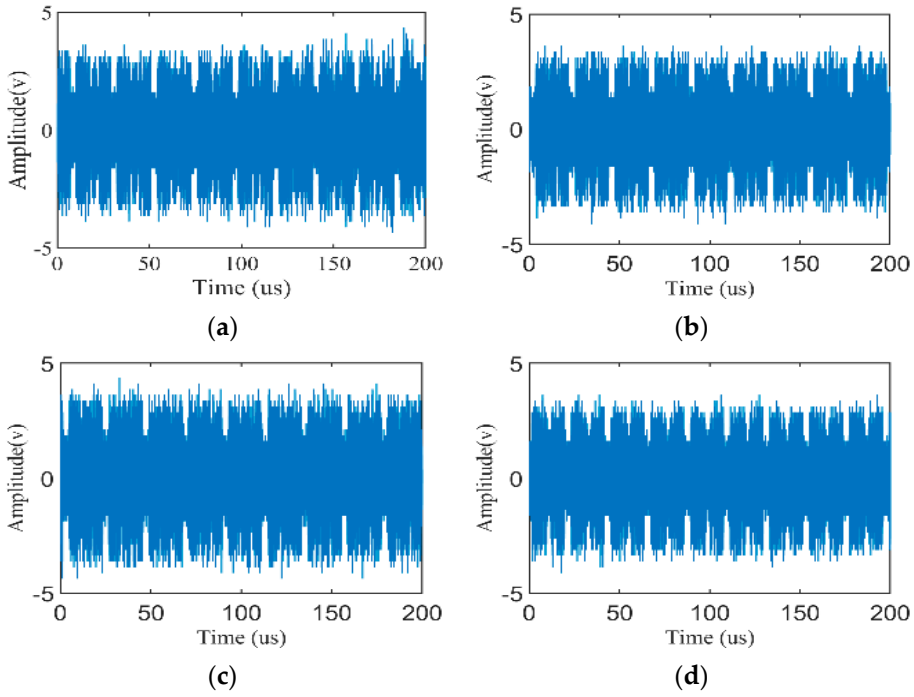

Figure 12. DSA collection results. (**a**–**d**) represent the results collected on the DSA after the four signals shown in Figure 10 pass through the delay optics RC.

3.2. Results

The results obtained from the reservoir layer are necessary to downsample the signal for each cycle. We chose a virtual node number of 200. We chose to perform equidistant sampling on the signal with 1,000,000 sampling points. Ultimately, each signal will consist of 200 points, as shown in Figure 13.

For the training algorithm, we first use linear regression to train the signals, with a sample size of 32 waveforms, i.e., eight samples for each type of waveform. We label the samples of the four types of waveforms with training labels 1–4 and then randomly divide them into 70% and 30% of the total samples as the training set and test set, respectively. First, we train the output weight W using the training set and then evaluate the output weight W using the test set. We plotted the true and predicted values of the test as shown in Figure 14.

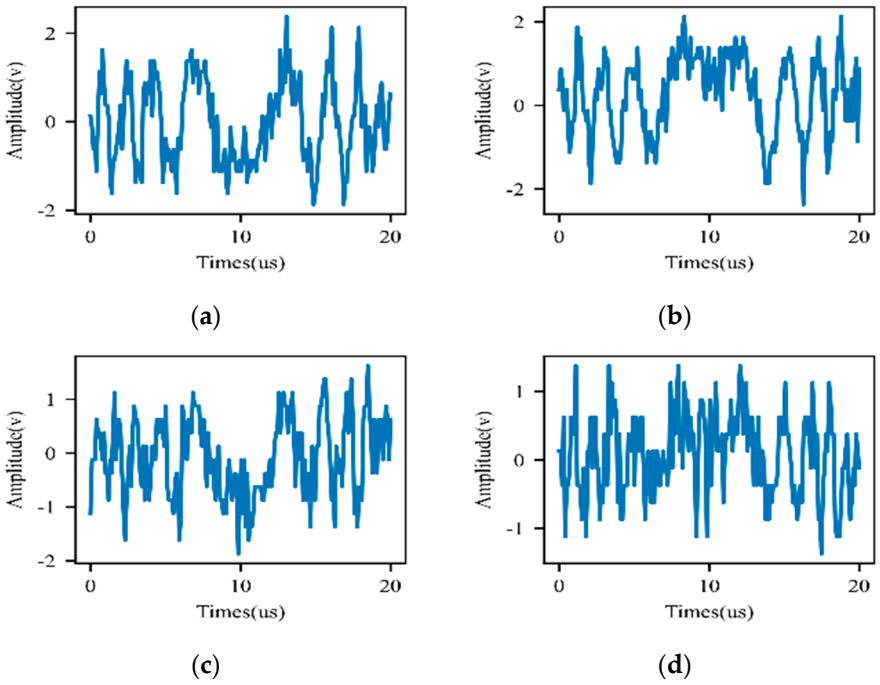

Figure 13. The virtual node status of four types of modulated signals. (**a**–**d**) represent the results after downsampling. This is the dataset that we need to train on the computer.

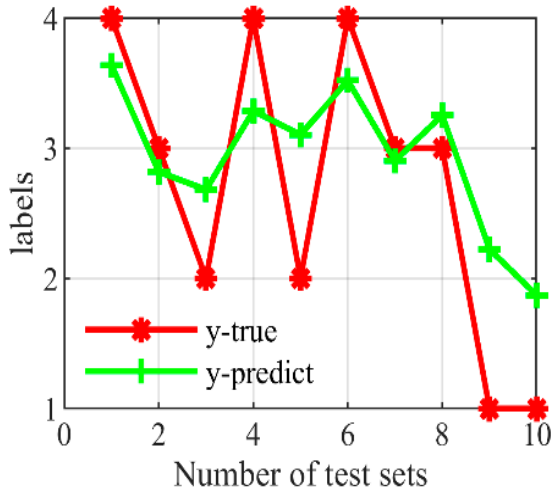

Figure 14. Classification results between true values and predicted values, based on linear regression training algorithm.

According to Figure 14, only 5 out of 10 signals can be successfully classified. The calculated NRMSE is approximately 0.23359. This proves that the linear regression algorithm has relatively poor results for the classification task of this experiment.

Next, we used the SVM algorithm to train and test the same dataset. As SVM is primarily used to solve data classification-related problems, we used a tool for evaluating the performance of classification models, the confusion matrix, to assess the results of this experiment. The confusion matrix was originally used to solve binary classification problems. For multi-classification problems, the representation of the confusion matrix remains the same, but the dimensions of the matrix will increase. Like before, we used 70% of the dataset for training and 30% for testing. The test results are shown in Figure 15.

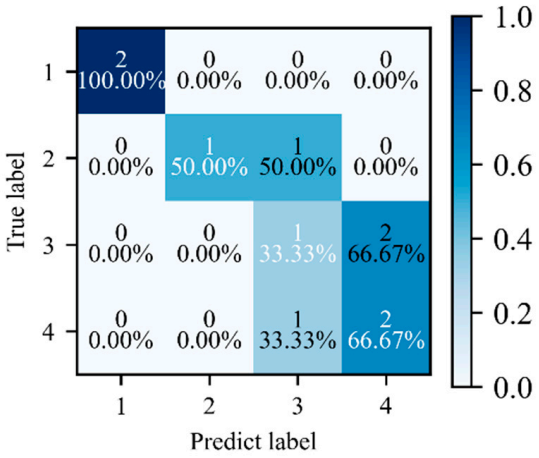

Figure 15. SVM recognition results.

As can be seen from Figure 15, among the 10 waveforms, one waveform 2 was identified as waveform 3, and two waveforms 3 were identified as waveform 4. One waveform 4 was identified as waveform 3. The overall accuracy rate was 60%, which is higher than the 50% accuracy rate of linear regression.

The training algorithm we finally adopted is Random Forest. The results of our test using the Random Forest algorithm are shown in Figure 16.

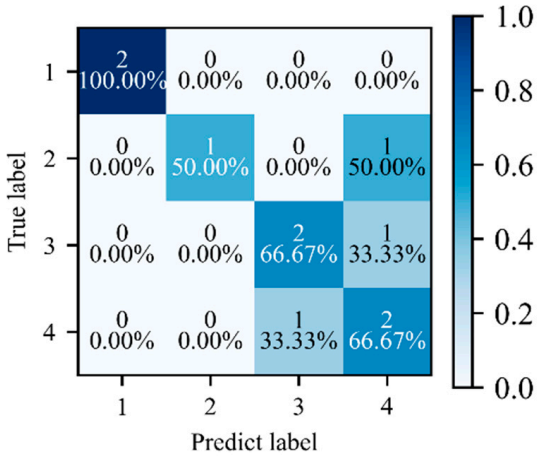

Figure 16. Random Forest recognition results.

As depicted in Figure 16, out of the 10 test samples, three signals were misidentified, resulting in an overall recognition accuracy of 70%. The recognition performance of the Random Forest algorithm is superior when compared to the Linear Regression algorithm and SVM.

In order to more accurately compare the recognition performance of the three algorithms, we decided to expand the dataset. The original 32 datasets were increased to 64. Linear regression, SVM, and random forest were then used to test and identify the test set, with the recognition results shown in Figure 17a–c. As can be discerned from Figure 17a–c, with the test samples doubled, the recognition accuracy of the three algorithms improved to varying degrees. Specifically, the linear regression algorithm achieved an accuracy of 70%, with a noticeable reduction in the error between the predicted and actual values, yielding an NRMSE of 0.1443. The recognition accuracy of the SVM algorithm is identical to that of the Random Forest algorithm, both reaching 90%. Only two instances of Waveform 4 were misidentified as Waveform 3.

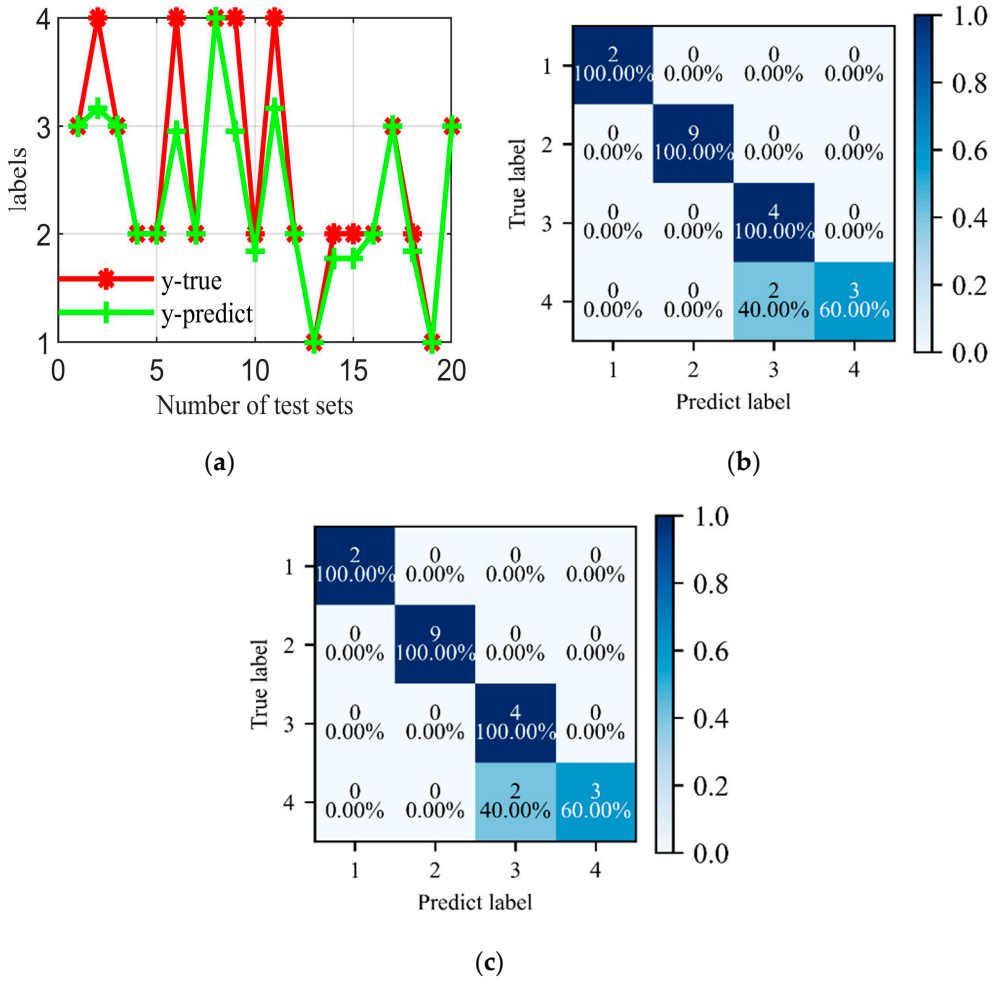

Figure 17. (**a**) Linear regression algorithm test results, (**b**) SVM algorithm test results, (**c**) Random forest algorithm test results.

We further increased the sample size by 32, bringing the total to 96. The test set consisted of 29 waveforms. The results obtained from testing the test set with the three algorithms were as follows: the accuracy of the linear regression algorithm was 93.1%, while both SVM and random forest achieved an accuracy of 100%. Instead of individually displaying the accuracy rates, we used a bar chart to compare the accuracy rates of the three algorithms with different sample sizes and error lines were added to each group of graphs to represent the performance differences between different datasets, with the value of the error line being the normalized mean square error of each training group. The comparison results are shown in Figure 18.

As evidenced by the accuracy comparison in Figure 18, the linear regression algorithm consistently had the lowest recognition accuracy in all three experiments, with a minimum of 50%. However, as the sample size increased, the accuracy peaked at 93.1%. Both SVM and Random Forest had the same recognition accuracy for medium and large sample sizes, particularly when the sample size was 96, where the recognition accuracy reached 100%. However, for smaller sample sizes, the recognition performance of SVM was inferior to that of the random forest algorithm. The reason is due to the inherent characteristics of the two algorithms. The SVM algorithm finds a hyperplane in the dataset to separate two different categories, making it more suitable for binary classification problems. When dealing with multi-classification problems, it needs to combine multiple binary classification models. On the other hand, the random forest algorithm classifies by constructing multiple decision tree models, making it more suitable for multi-classification tasks. Therefore, when dealing

with small sample datasets, the classification effect of SVM is not as good as that of the random forest algorithm.

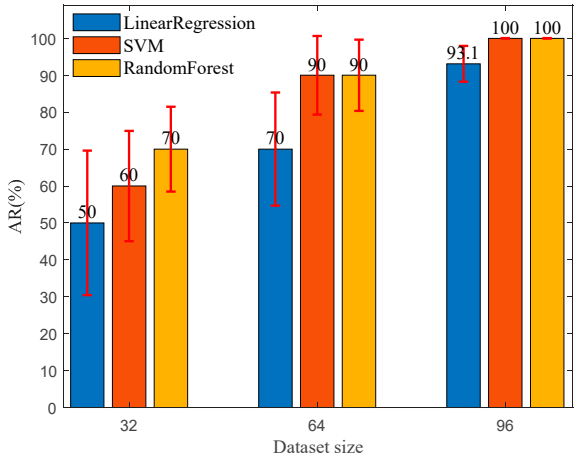

Figure 18. The recognition accuracy of three algorithms under different dataset sizes.

The RC system built in this experiment has certain generalization capabilities and robustness. This is because the reservoir can classify the responses generated by the same and similar input signals. After the same and similar input signals undergo nonlinear mapping through the reservoir layer, they can still maintain their similarity, have similar output dynamics, and are not linearly separated. This nonlinear mapping is accomplished by the nonlinear device DFB laser. The electronic equipment used in the experiment inevitably also brings certain noise interference, such as AWG and DSA. Practical results show that RC is not sensitive to unnecessary minor fluctuations (such as noise) and can classify the same and similar input signals into the same category.

4. Conclusions

In this paper, we investigated the factors influencing the recognition accuracy of different training algorithms based on delay-optical RC and successfully identified the FMCW LIDAR signal. At the output layer, we employed three different algorithms to identify FMCW LiDAR signals at four different distances and tested and validated them using three different sizes of datasets. The number of signals in the datasets for this experiment was 32, 64, and 96, respectively. The accuracy of signal recognition by the linear regression algorithm was 50%, 70%, and 93.1%, respectively. The accuracy of signal recognition by the SVM algorithm was 60%, 90%, and 100%, respectively. The accuracy of signal recognition by the random forest algorithm was 70%, 90%, and 100%, respectively.

Based on the experimental results, we can draw three conclusions: (1) The optical RC system based on time delay can accurately identify FMCW LiDAR signals at different distances, providing a new approach for the recognition of FMCW LiDAR signals. (2) In the FMCW LiDAR signal recognition task, regardless of the size of the dataset samples, the recognition accuracy of nonlinear algorithms is higher than that of linear algorithms. This is because linear algorithms are more suitable for time series prediction tasks, while nonlinear algorithms are more suitable for classification tasks. (3) When the number of samples is not large, the recognition effect of the random forest algorithm in nonlinear algorithms is better than that of SVM. This is because the random forest is an ensemble learning method that integrates multiple decision trees to make predictions. When making predictions, the random forest will consider the prediction results of all decision trees and then choose the most frequent result as the final prediction result. Since SVM is essentially a binary classification model, the random forest will perform better in multi-classification tasks.

Our research provides another approach to improving the accuracy of signal recognition for tasks based on delay-optical RC, not only limited to the study of optical devices

but also improving the algorithm. As we mentioned earlier, the delay-based optical RC system we built has certain generalization capabilities. The RC system is capable of handling various types of time-series signals, not just specific types of signals. This allows the RC system to be applicable in a variety of different application scenarios. Of course, the research on delay-optical RC is far from over. Current implementations of reservoir computing hardware generally require the preprocessing of signals and post-processing steps for algorithm training on collected data. How to decouple from the computer, implement all-optical reservoir computing that can be trained online, and design the reservoir according to specific tasks are directions worth researching in the future. The success of our simultaneous experiment also provides new ideas for the processing of FMCW LiDAR signals, which has potential application prospects for LiDAR in the fields of automatic vehicles and distance measurement.

Author Contributions: Conceptualization, T.L. and R.Z.; methodology, R.Z. and S.L.; software R.Z.; validation, R.Z. and C.W.; formal analysis, A.Z. and R.Z.; investigation, R.Z. and C.W.; data management, T.L., R.Z. and C.W.; writing—original draft preparation, A.Z.; writing—review and editing, R.Z. and T.L.; visualization, R.Z.; supervision, C.W. and A.Z. All authors have read and agreed to the published version of the manuscript.

Funding: This research received no external funding.

Data Availability Statement: The original contributions presented in the study are included in the article, further inquiries can be directed to the corresponding author.

Conflicts of Interest: The authors declare no conflicts of interest.

References

1. Hochreiter, S. Untersuchungen zu dynamischen neuronalen Netzen. *Diploma Tech. Univ. München* **1991**, *91*, 31.
2. Jaeger, H. The "echo state" approach to analysing and training recurrent neural networks-with an erratum note. *Bonn Ger. Ger. Natl. Res. Cent. Inf. Technol. GMD Tech. Rep.* **2001**, *148*, 13.
3. Maass, W.; Natschläger, T.; Markram, H. Real-time computing without stable states: A new framework for neural computation based on perturbations. *Neural Comput.* **2002**, *14*, 2531–2560. [CrossRef] [PubMed]
4. Verstraeten, D.; Schrauwen, B.; D'Haene, M.; Stroobandt, D. An experimental unification of reservoir computing methods. *Neural Netw.* **2007**, *20*, 391–403. [CrossRef] [PubMed]
5. Mujal, P.; Martínez-Peña, R.; Giorgi, G.L.; Soriano, M.C.; Zambrini, R. Time-series quantum reservoir computing with weak and projective measurements. *npj Quantum Inf.* **2023**, *9*, 16. [CrossRef]
6. Ibrahim, H.; Loo, C.K.; Alnajjar, F. Speech emotion recognition by late fusion for bidirectional reservoir computing with random projection. *IEEE Access* **2021**, *9*, 122855–122871. [CrossRef]
7. Tanaka, G.; Nakane, R. Simulation platform for pattern recognition based on reservoir computing with memristor networks. *Sci. Rep.* **2022**, *12*, 9868. [CrossRef] [PubMed]
8. Palumbo, F.; Gallicchio, C.; Pucci, R.; Micheli, A. Human activity recognition using multisensor data fusion based on reservoir computing. *J. Ambient Intell. Smart Environ.* **2016**, *8*, 87–107. [CrossRef]
9. Yue, D.; Hou, Y.; Hu, C.; Zang, C.; Kou, Y. Handwritten Digits Recognition Based on a Parallel Optoelectronic Time-Delay Reservoir Computing System. *Photonics* **2023**, *10*, 236. [CrossRef]
10. Picco, E.; Massar, S. Real-Time Photonic Deep Reservoir Computing for Speech Recognition. In Proceedings of the 2023 International Joint Conference on Neural Networks (IJCNN), Gold Coast, Australia, 18–23 June 2023; pp. 1–7.
11. Lukoševičius, M. A practical guide to applying echo state networks. In *Neural Networks: Tricks of the Trade*, 2nd ed.; Springer: Berlin/Heidelberg, Germany, 2012; pp. 659–686.
12. Bianchi, F.M.; Scardapane, S.; Løkse, S.; Jenssen, R. Reservoir computing approaches for representation and classification of multivariate time series. *IEEE Trans. Neural Netw. Learn. Syst.* **2020**, *32*, 2169–2179. [CrossRef]
13. Jin, Y.; Zhao, Q.; Yin, H.; Yue, H. Handwritten numeral recognition utilizing reservoir computing subject to optoelectronic feedback. In Proceedings of the 2015 11th International Conference on Natural Computation (ICNC), Zhangjiajie, China, 15–17 August 2015; pp. 1165–1169.
14. Wan, L.; Zeiler, M.; Zhang, S.; Le Cun, Y.; Fergus, R. Regularization of neural networks using dropconnect. In Proceedings of the International Conference on Machine Learning, Atlanta, GA, USA, 16–21 June 2013; pp. 1058–1066.
15. Bianchi, F.M.; Scardapane, S.; Uncini, A.; Rizzi, A.; Sadeghian, A. Prediction of telephone calls load using echo state network with exogenous variables. *Neural Netw.* **2015**, *71*, 204–213. [CrossRef] [PubMed]
16. Bush, K.; Anderson, C. Modeling reward functions for incomplete state representations via echo state networks. In Proceedings of the 2005 IEEE International Joint Conference on Neural Networks, Montreal, QC, Canada, 31 July–4 August 2005; pp. 2995–3000.

17. Babinec, Š.; Pospíchal, J. Merging echo state and feedforward neural networks for time series forecasting. In Proceedings of the Artificial Neural Networks–ICANN 2006: 16th International Conference, Athens, Greece, 10–14 September 2006; pp. 367–375.
18. Bianchi, F.M.; Scardapane, S.; Løkse, S.; Jenssen, R. Bidirectional deep-readout echo state networks. *arXiv* **2017**, arXiv:1711.06509.
19. Kuriki, Y.; Nakayama, J.; Takano, K.; Uchida, A. Impact of input mask signals on delay-based photonic reservoir computing with semiconductor lasers. *Opt. Express* **2018**, *26*, 5777–5788. [CrossRef] [PubMed]
20. Bueno, J.; Brunner, D.; Soriano, M.C.; Fischer, I. Conditions for reservoir computing performance using semiconductor lasers with delayed optical feedback. *Opt. Express* **2017**, *25*, 2401–2412. [CrossRef] [PubMed]
21. Hülser, T.; Köster, F.; Jaurigue, L.; Lüdge, K. Role of delay-times in delay-based photonic reservoir computing. *Opt. Mater. Express* **2022**, *12*, 1214–1231. [CrossRef]
22. Brigham, E.O.; Morrow, R. The fast Fourier transform. *IEEE Spectr.* **1967**, *4*, 63–70. [CrossRef]
23. Yue, Y.; Mididoddi, C.K.; Jing, N.; Wang, C. Reservoir computing assisted ultrafast user localization in beam steering optical wireless system. *IEEE Photonics Technol. Lett.* **2021**, *33*, 1030–1033. [CrossRef]
24. Yu, K.; Qi, Y.; Shen, L.; Wang, X.; Quan, D.; Zhang, D. Radar Signal Recognition Based on Bagging SVM. *Electronics* **2023**, *12*, 4981. [CrossRef]
25. Tian, L.; Zeng, Z.; Li, Z.; Liu, C. Radar signal recognition method based on Random Forest model. In Proceedings of the 2022 3rd International Conference on Big Data, Artificial Intelligence and Internet of Things Engineering (ICBAIE), Xi'an, China, 15–17 July 2022; pp. 98–102.
26. Pierrottet, D.; Amzajerdian, F.; Petway, L.; Barnes, B.; Lockard, G.; Rubio, M. Linear FMCW laser radar for precision range and vector velocity measurements. *MRS Online Proc. Libr. (OPL)* **2008**, *1076*, 1076-K04. [CrossRef]
27. Guo, Z.; Han, G.; Yan, J.; Greenwood, D.; Marco, J.; Yu, Y. Ultimate Spatial Resolution Realisation in Optical Frequency Domain Reflectometry with Equal Frequency Resampling. *Sensors* **2021**, *21*, 4632. [CrossRef]
28. Xing, J.; Zhang, Y.; Wang, F.; Feng, K.; Zhang, Y.; Yan, Z.; Zhang, X. A Method Based on Time-Scale Factor for Correcting the Nonlinear Frequency Sweeping in an OFDR System. *IEEE Photonics J.* **2019**, *11*, 1–8. [CrossRef]
29. Iiyama, K.; Yasuda, M.; Takamiya, S. Extended-range high-resolution FMCW reflectometry by means of electronically frequency-multiplied sampling signal generated from auxiliary interferometer. *IEICE Trans. Electron.* **2006**, *89*, 823–829. [CrossRef]
30. Jiang, S.; Liu, B.; Wang, S. A Dispersion Compensation Method Based on Resampling of Modulated Signal for FMCW Lidar. *Sensors* **2021**, *21*, 249. [CrossRef]
31. Vergnole, S.; Lévesque, D.; Lamouche, G. Experimental validation of an optimized signal processing method to handle non-linearity in swept-source optical coherence tomography. *Opt. Express* **2010**, *18*, 10446–10461. [CrossRef]
32. Appeltant, L.; Soriano, M.C.; Van der Sande, G.; Danckaert, J.; Massar, S.; Dambre, J.; Schrauwen, B.; Mirasso, C.R.; Fischer, I. Information processing using a single dynamical node as complex system. *Nat. Commun.* **2011**, *2*, 468. [CrossRef]